Reduced turbulent transport in the quasi-isodynamic stellarator configuration CIEMAT-QI4

J. M. García-Regaña, I. Calvo, E. Sánchez, H. Thienpondt, J. L. Velasco and J. A. Capitán

Laboratorio Nacional de Fusión, CIEMAT, 28040 Madrid, Spain

E-mail: `jose.regana@ciemat.es`

August 2017

Abstract. CIEMAT-QI4 is a quasi-isodynamic stellarator configuration that simultaneously features very good fast-ion confinement in a broad range of β values, low neoclassical transport and bootstrap current, and ideal magnetohydrodynamic stability up to $\beta = 5\%$. In this paper it is shown that CIEMAT-QI4 also exhibits reduced turbulent transport. This is demonstrated through nonlinear electrostatic simulations with the gyrokinetic code `stella`, including kinetic ions and electrons. The relation between reduced turbulent transport and the fact that CIEMAT-QI4 very approximately satisfies the so-called maximum-J property is discussed.

1. Introduction

In stellarators [1], the magnetic field is generated by means of external coils. This prevents current-driven instabilities and makes steady-state operation easier compared with the tokamak, whose axisymmetric magnetic field is created, in part, by driving a large toroidal current in the plasma. This basic difference on how the magnetic field is produced is the reason why the stellarator is an attractive potential alternative to the tokamak concept for fusion power plants. However, the generation of the field exclusively by external magnets implies that stellarator configurations are inherently three-dimensional and, in general, do not enjoy the excellent confinement properties that are intrinsic to tokamaks thanks to axisymmetry. For a stellarator to exhibit confinement levels comparable to the tokamak, its magnetic field must be carefully tailored in a process known as stellarator optimization.

One approach to optimization consists of looking for three-dimensional magnetic fields such that the magnetic field strength, in certain sets of coordinates, possesses a symmetry direction. These magnetic fields are called quasisymmetric. In exactly quasisymmetric stellarators, like in a tokamak, all collisionless orbits are confined. The Helically Symmetric eXperiment (HSX) [2] and the design of the National Compact Stellarator Experiment (NCSX) [3] provide examples of stellarator magnetic fields optimized looking for quasisymmetry. More recently, magnetic fields extremely close to exact quasisymmetry have been obtained [4].

The approach followed in the design of Wendelstein 7-X (W7-X), the first large optimized stellarator, is different and is based on the concept of quasi-isodynamicity. A magnetic field is quasi-isodynamic if, without necessarily exhibiting explicit symmetries, it satisfies two properties: all collisionless orbits are confined and magnetic-field-strength contours are poloidally closed. Exact quasi-isodynamicity guarantees a neoclassical transport level similar to that of tokamaks and vanishing bootstrap current [5].

The neoclassical optimization of W7-X has been experimentally demonstrated [6], representing an enormous success and a key milestone for the stellarator research programme. The possibility to control the size of the toroidal plasma current, important to preserve the island structure on which the divertor of W7-X is based, has also been proven [7]. However, the optimization of W7-X is insufficient with respect to two critical aspects in the path towards stellarator reactors: fast-ion confinement and turbulent transport. In a reactor, even a small fraction of alpha particles lost before thermalization could severely damage the wall, but W7-X was not designed to confine fast ions at low normalized plasma pressure, β, and the situation is expected to improve only moderately at high β (see e.g. [8]). As for turbulent transport, this was not a feasible optimization target when W7-X was designed, whereas the first experimental campaigns have shown that turbulence can dominate transport across the entire plasma radius and can contribute to the clamping of the core ion temperature [9].

Over the last few years, thanks to theory developments and increased computational capabilities, significant progress has been made in the quest for the next generation of quasi-isodynamic configurations. A number of new techniques and codes have been devised to produce configurations that are close to quasi-isodynamicity [10, 11, 12, 13, 14]. Among all these efforts, we focus in the present work on the configuration CIEMAT-QI4, presented in [10]. CIEMAT-QI4 is optimized with respect to fast-ion confinement in a broad range of β values and, at the same time, is ideal MHD stable, and gives low neoclassical transport and bootstrap current. All these physics aspects are extensively covered in [10]. Here, we further characterize the physics performance of this configuration by presenting an initial analysis of its turbulent transport. It is worth-noting that CIEMAT-QI4 belongs to the familiy of quasi-isodynamic configurations with flat mirror term‡, which naturally tend to satisfy the maximum-J property at low β [15]. This property entails that the second adiabatic invariant§, J, is constant on magnetic surfaces and decreases monotonically with the radius. The maximum-J property has been argued to be beneficial for mitigating turbulence stemming from trapped electron modes driven by density gradients and other ion-scale gyrokinetic instabilities involving kinetic electrons [16, 17, 18, 19]. Consistent with these expectations, we confirm in the present work that turbulent transport in CIEMAT-QI4 is reduced with respect to W7-X.

The rest of the paper is organized as follows. In section 2, we describe the configuration CIEMAT-QI4. For comparison, specifics of the standard configuration of Wendelstein 7-X (W7-X) at the same value of β are also provided. In section 3 the turbulence results for CIEMAT-QI4 and W7-X, obtained with the gyrokinetic code `stella`, are analysed. For the case of CIEMAT-QI4, the results are expanded by considering three other β values, as the maximum-J property is more closely fulfilled with increasing β.

‡ The mirror term for a quasi-isodynamc configuration is defined in [15] as $\sum_{n>0} B_{0n}$, where B_{mn} are the modes of the Fourier expansion of the magnetic field strength expressed in Boozer coordinates, m is the poloidal number and n is the toroidal number.

§ The second adiabatic invariant, J, is defined for trapped particles as $J = \oint v_{||} \mathrm{d}l$, where the integral is taken over the trapped orbit, $v_{\|}$ is the parallel velocity and l is the arc length along magnetic field lines.

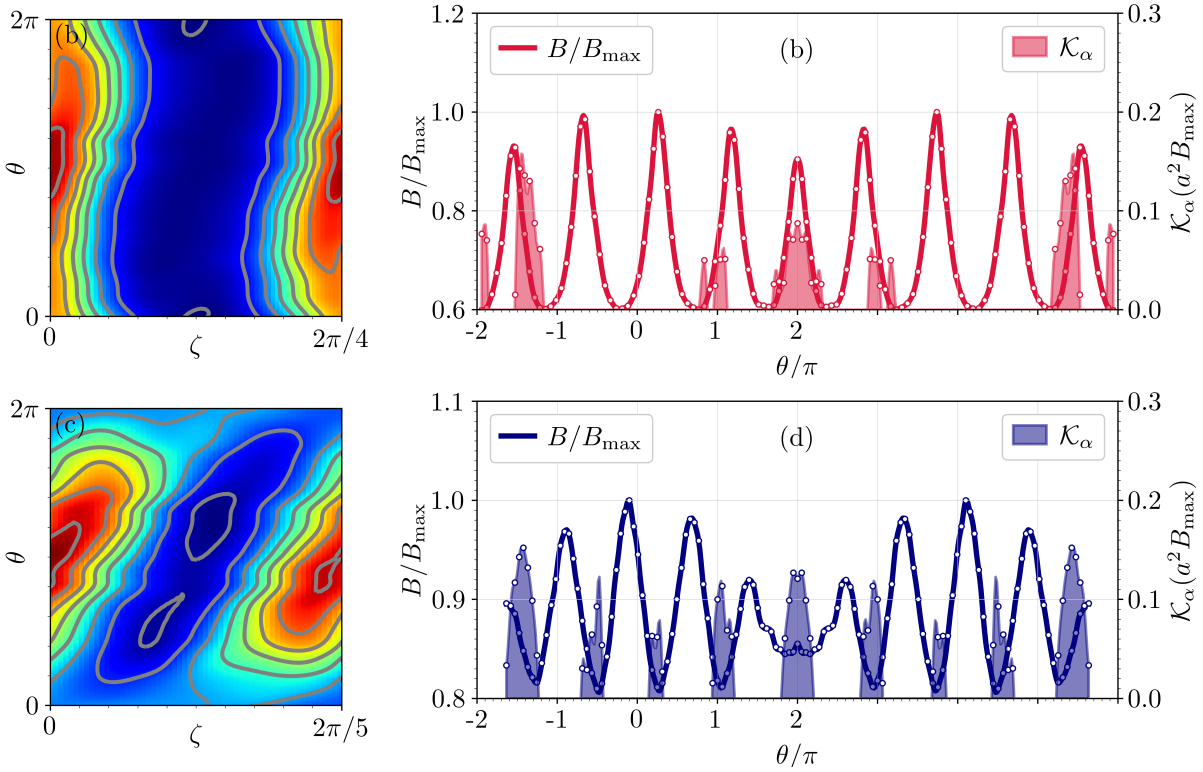

Figure 1. Magnetic field strength, B, of CIEMAT-QI4 (a) and W7-X (c), both at $\beta = 1.5\%$ and at $r/a = 0.7$, where red and blue tones represent, respectively, higher and lower values. Magnetic field strength (solid line) and bad curvature regions (shaded areas) as a function of the poloidal coordinate for CIEMAT-QI4 (b) and W7-X (d). The markers represent the parallel grid points used in the nonlinear simulations.

Finally, conclusions are summarised in section 4.

2. The magnetic configuration CIEMAT-QI4

CIEMAT-QI4 is a 4-field-period configuration with aspect ratio $A \approx 10$ that has been obtained using the optimization suite of codes STELLOPT [20]. The code KNOSOS [21] has been integrated into STELLOPT and employed to compute novel orbit-averaged quantities that are used as proxies for the optimization of fast-ion confinement [8]. More details of the optimization runs, target function and proxies can be found in [10]. An aspect not considered explicitly in the STELLOPT optimization loop that led to CIEMAT-QI4 is turbulent transport. That is the central aspect addressed in this work.

While the characteristics of CIEMAT-QI4 are very good in a broad range of β values, $\beta = 1.5\%$ is the value of β for which the configuration was optimised (here, β is a volume-averaged quantity, obtained considering parabolic plasma pressure values). For that case, the magnetic field strength B in one period is represented in figure 1(a) for the radial position $r/a = 0.7$, which is considered in the turbulence simulations presented in section 3. Here, r is the effective minor radius coordinate and a is its value at the last closed flux surface. In figure 1(b) the magnetic field strength is also depicted along the magnetic field line $\alpha = 0$, extended approximately two poloidal turns, used for the flux tube simulations discussed in section 3. Here $\alpha = \theta - \iota\zeta$ labels magnetic field lines, θ and ζ are, respectively, the poloidal and toroidal angular flux PEST [22] coordinates, and the field line is centered with respect to the point $(\theta, \zeta) = (0, 0)$, corresponding to the outboard mid-plane at the bean-shaped poloidal cross section. On the other hand, $\mathcal{K}_\alpha = (\mathbf{b} \times \nabla B) \cdot \nabla\alpha/\psi_t'$ is a geometric coefficient related to magnetic and curvature drifts. Microinstabilities are prone to localise where $\mathcal{K}_\alpha > 0$, a condition that defines what are usually known as bad curvature regions. Here, $\mathbf{b}$ is a unit vector pointing in the direction of the magnetic field and ψ_t' the radial derivative of the toroidal flux. For this equilibrium, generated with the code `VMEC` [23], the shaded areas in figure 1(b) indicate regions of bad curvature. For comparison, in figures 1(c) and 1(d), the equivalent two plots are presented for the standard (or EIM) W7-X configuration, also at $\beta = 1.5\%$. Within the broad space of W7-X configurations, the standard configuration is generated by a set of modular coils, all of them carrying the same current. This is similar to the case of CIEMAT-QI4, as described in [10], where a preliminary coil set is

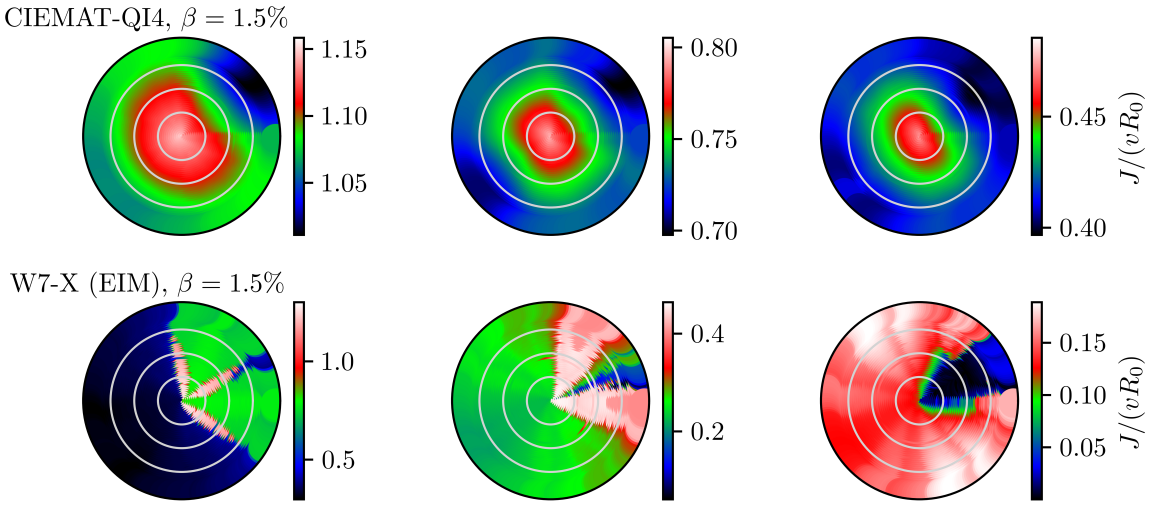

Figure 2. Second adiabatic invariant, J, for CIEMAT-QI4 (top row) and W7-X (EIM) (bottom row), both at $\beta = 1.5\%$. From left to right, the plots correspond to representative examples of barely (left), moderately (center) and deeply (right) trapped particles. For this representation $(r/a)^2$ and α are used as radial and angular, respectively, polar coordinates. The circular contours represent the flux surfaces $(r/a)^2 = \{0.25, 0.5, 0.75\}$. Note that in this polar representation α is defined in terms of the Boozer, instead of PEST, angular coordinates.

presented. The neoclassical optimization of W7-X (one of its main design objectives) has been experimentally demonstrated in the standard configuration, resulting in record values of the fusion triple product in stellarator plasmas [6].

To the naked eye, by observing the presence of poloidally closed contours in CIEMAT-QI4 in figure 1(a) and the clear alignment of maxima and minima of B in figure 1(b), in contrast with the equivalent W7-X figures 1(c) and 1(d), one can guess the different degree of quasi-isodynamicity of the two configurations. As for the coefficient $\mathcal{K}_\alpha$, while W7-X exhibits a noticeable overlap of magnetic field wells and bad curvature regions, usually identified as the origin of trapped-particle-driven instabilities, in CIEMAT-QI4 the overlap is much smaller.

The maximum-J property is normally invoked in the context of turbulence studies when it comes to arguing the resilience of the configurations to turbulence driven by trapped-electron-modes (TEM) and other ion-scale instabilities involving kinetic electrons [16, 17, 18, 19]. This property implies that the second adiabatic invariant J is constant on magnetic surfaces and monotonically decreasing along the radius. In figure 2, depicting J as a function of α and r for CIEMAT-QI4 and for the standard configuration of W7-X, it can be observed that the maximum-J property holds very closely in CIEMAT-QI4. The reason is that so-called flat mirror configurations (a notion introduced and developed in [15]) such as CIEMAT-QI4 tend to make $\partial_r J < 0$ for all trapped particles even for low β values.

In summary, the CIEMAT-QI4 geometric properties support the hypothesis of less detrimental turbulent transport and enhanced resilience to certain microinstabilities. This will be confirmed in section 3 by means of nonlinear gyrokinetic simulations.

3. Turbulent transport in CIEMAT-QI4

Turbulence studies in stellarators have proliferated in recent years with the arrival of new codes [24, 25, 26], the increase in computational capability, and the evidence that once neoclassical transport is optimised, turbulence comes to explain a good part of experimental observations. For instance, taking W7-X as a paradigmatic case of the latter, turbulence simulations have explained why neither core density depletion [27] nor the accumulation of impurities [28, 29], predicted by neoclassical theory, take place in standard scenarios. Moreover, the remarkable reduction of heat fluxes with increasing density gradient in W7-X [30] aligns with the experimental evidence that increasing the bulk density peaking is crucial to achieve high performance [31]. This section addresses the dependence of turbulent fluxes on the density gradient, by means of nonlinear `stella` simulations, aiming to assess whether in CIEMAT-QI4 this advantageous characteristic of W7-X is preserved and even improved.

The nonlinear simulations performed with the code `stella`, are electrostatic, collisionless and

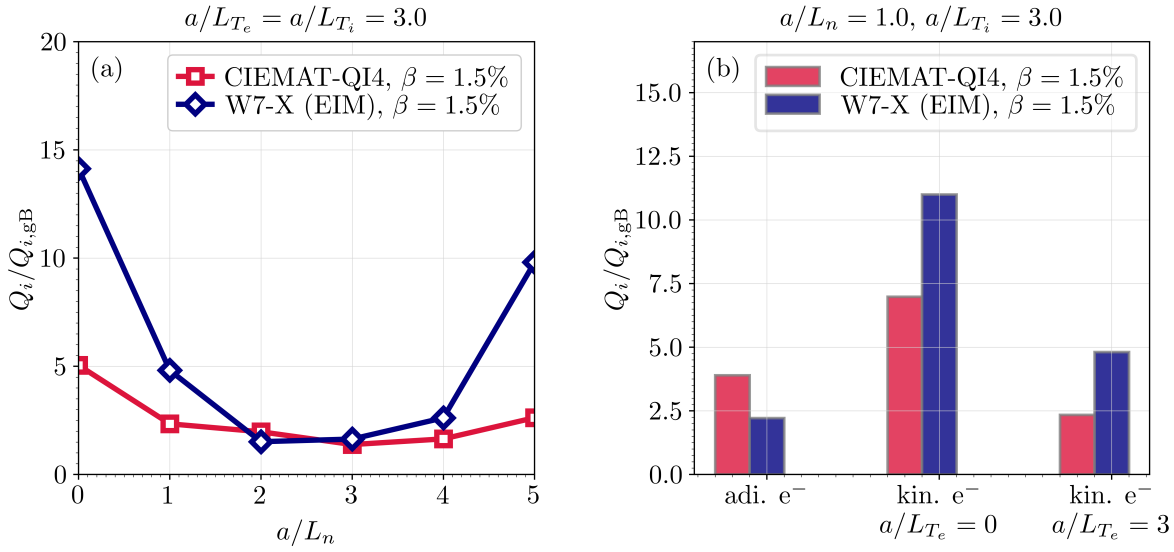

Figure 3. (a) Ion heat flux as a function of the normalized density gradient for CIEMAT-QI4 (squares) and W7-X (diamonds), both configurations at $\beta = 1.5\%$. (b) Ion heat flux for CIEMAT-QI4 and W7-X in the case where $a/L_n = 1.0$ and electrons are assumed adiabatic (left pair of bars), kinetic with vanishing temperature gradient (central pair of bars) and kinetic with finite temperature gradient (pair of bars on the right). Throughout this work the ion and electron heat fluxes are normalised to the gyro-Bohm heat flux of the ions $Q_{i,\mathrm{gB}} = (\rho_i/a)^2 n_i T_i v_{\mathrm{th},i}$

consider a flux tube centered around the magnetic field line $\alpha_0 = 0$, which lies on the flux surface at $r_0/a = 0.7$ (the subindex 0 denotes quantities evaluated on the considered field line). All simulations are performed with kinetic ions and electrons, unless stated otherwise. For this radial position and field line, the magnetic field strength and geometric coefficient $\mathcal{K}_\alpha$ for both configurations have already been presented in figure 1 and discussed in section 2. Both configurations have low global magnetic shear, $\hat{s}$, over practically their entire radius and, for the specific radial position chosen, $\hat{s} = -0.110$ for W7-X and $\hat{s} = -0.022$ for CIEMAT-QI4. Due to the low shear of both configurations, the generalised twist and shift boundary conditions, proposed in [32], have been employed, extending the flux tube up to 10.4 and 9.0 toroidal field periods in W7-X and CIEMAT-QI4, respectively, which corresponds to approximately two poloidal turns. These lengths ensure that, considering the aforementioned boundary conditions, the width of the flux tube is equal along the radial, $x = (r - r_0)$, and in binormal, $y = r_0(\alpha - \alpha_0)$, coordinates. In other words, the shortest wavevectors (large scales) in these two directions are set to $k_{x,\mathrm{min}} = k_{y,\mathrm{min}} = 0.067\rho_i^{-1}$ (which correspond to the lengths $l_x = l_y = 94.2\rho_i$). The smallest scales simulated are those with $k_{x,\mathrm{max}} = k_{y,\mathrm{max}} = 3.0\rho_i^{-1}$. With regard to the rest of parameters of the simulations, the magnetic field line is sampled by 64 points per poloidal turn, and the number of grid points in velocity space have been set to $N_\mu = 12$ grid points in the magnetic moment, μ, and $N_{v_\parallel} = 65$ in the parallel velocity coordinate, $v_\parallel$. Here, $\rho_i = v_{\mathrm{th},i}/\Omega_i$ is the thermal ion Larmor radius, $v_{\mathrm{th},i} = \sqrt{2T_i/m_i}$ is the thermal speed, $\Omega_i = eB_r/m_i$ is the gyrofrequency, e is the unit charge, m_i is the ion mass, T_i is the ion temperature and B_r is a reference magnetic field (see [24, 33], for further details on the electrostatic collisionless system of gyrokinetic equations solved by `stella`, coordinates used, geometry treatment and normalization conventions).

As we said above, we have carried out a scan in the density gradient, a/L_n, at finite electron and ion temperature gradients $a/L_{T_i} = a/L_{T_e} = 3.0$. Here, $a/L_X = -(a/X)\mathrm{d}X/\mathrm{d}r$ is the characteristic radial variation length scale, also referred to as the normalised gradient, of a given plasma profile $X(r)$. At the selected radial position, temperature gradients are typically around the value indicated above in standard ECRH and ECRH+NBI W7-X plasmas, whereas in enhanced performance discharges they can be larger. Regarding a/L_n, W7-X exhibits core values in the range of approximately $0.5 - 3$, depending on the scenario [34]. However, recent discharges have shown larger values during pure NBI phases [35].

The results of these scans in a/L_n for the ion heat flux, Q_i, are shown in figure 3(a) for the two configurations. In this figure, one can clearly observe how CIEMAT-QI4 at low density gradients exhibits appreciably lower Q_i values than in W7-X. Specifically, for the case $a/L_n = 0$, the ion heat flux is approximately 2.8 times lower than for W7-X, and for $a/L_n = 1$, the reduction reaches a factor

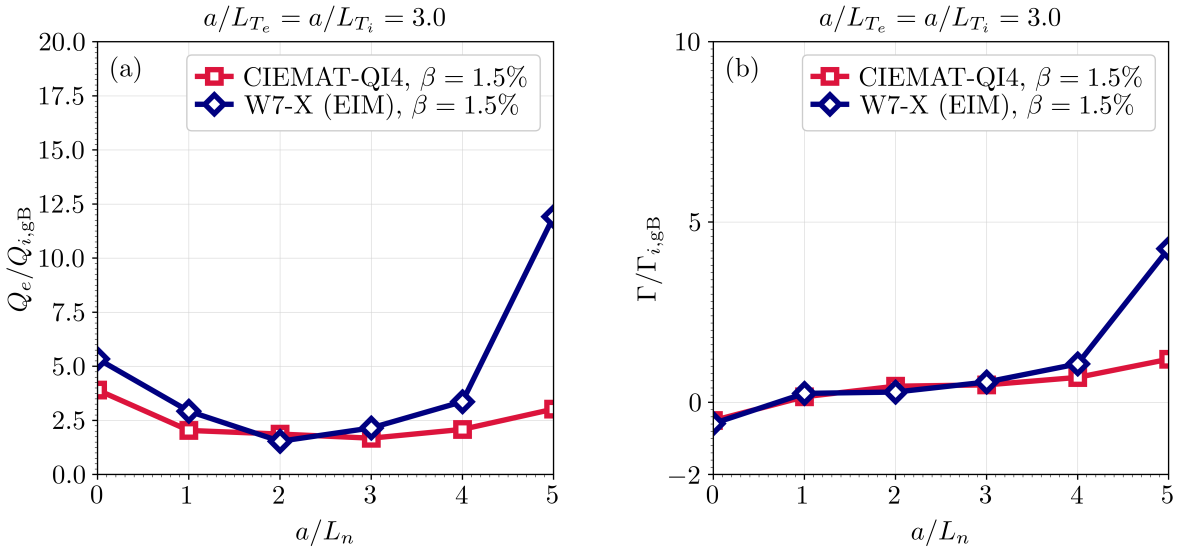

Figure 4. (a) Electron heat flux and particle flux (b) as a function of the normalised density gradient for CIEMAT-QI4 (squares) and W7-X standard configuration (diamonds), both at $\beta = 1.5\%$. The particle flux is normalised to the giro-Bohm value referred to the ions, $\Gamma_{i,gB} = n_i v_{th,i} (\rho_i/a)^2$.

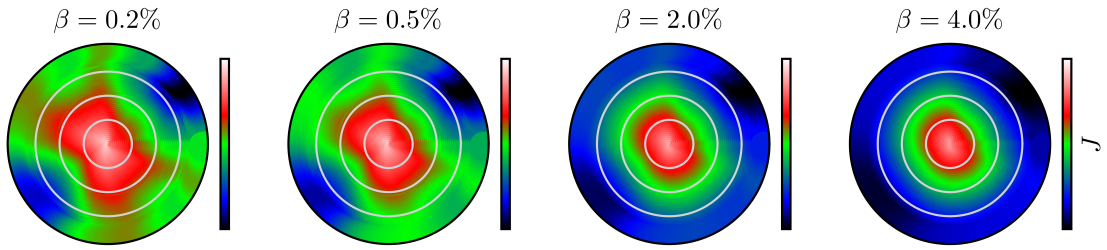

Figure 5. Second adiabatic invariant, J, for CIEMAT-QI4 at different values of β. For this representation, $(r/a)^2$ and α are used as radial and angular, respectively, polar coordinates. The circular contours represent the flux surfaces $(r/a)^2 = \{0.25, 0.5, 0.75\}$.

of nearly 2.0. Towards higher density gradient values ($a/L_n = 0 \to 2$), W7-X exhibits the Q_i reduction reported in [30, 36], following a mild increase of Q_i in the transition $a/L_n = 2 \to 4$, and a very pronounced growth for $a/L_n = 4 \to 5$. In contrast, CIEMAT-QI4 maintains a consistently low ion heat flux throughout the scanned density gradients. Thus, the ion heat flux level is low and robust to increasing a/L_n, with only a mild increase when a/L_n becomes the largest in all the represented range. In summary, CIEMAT-QI4 starts with significantly lower Q_i than W7-X when the density gradient is low, is comparable to W7-X at intermediate a/L_n values, and withstands the impact of moderate to very high values of a/L_n.

The better performance of CIEMAT-QI4 against W7-X for moderate to high density gradients, away from the low density gradient region where ITG is most unstable, is likely due to the diminsihed role predicted by theory of electron-driven instabilities in configurations that approach the maximum-J property. However, it is important to note that in the low density gradient region, the comparison just discussed involves electrons as well. Focusing on the case $a/L_n = 1$, in figure 3(b) the ion heat flux is shown in the case where electrons are considered adiabatic, kinetic with zero temperature gradient ($a/L_{T_e} = 0$), and kinetic with finite temperature gradient ($a/L_{T_i} = a/L_{T_e} = 3.0$). It can be seen that both W7-X and CIEMAT-QI4 experience an increase in ion heat flux when kinetic electrons are added, even with vanishing electron temperature gradient ($a/L_{T_e} = 0$). Among the two devices, the increase in the ion heat flux, already known in the literature [18], is much more pronounced in W7-X. Adding the temperature gradient to kinetic electrons makes the heat flux decrease, much more for CIEMAT-QI than for W7-X.

Turning back to the density gradient scan with kinetic electrons and all drives, in figures 4(a) and

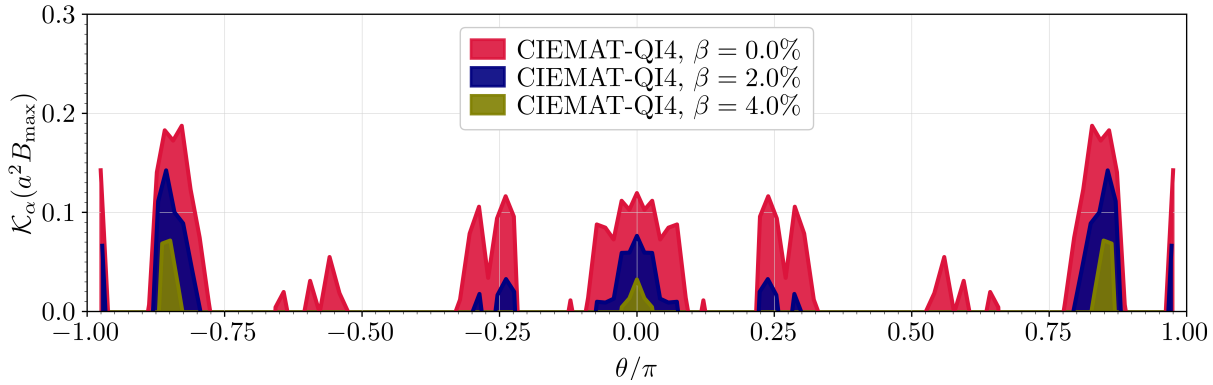

Figure 6. Regions of bad curvature ($\mathcal{K}_\alpha > 0$) along the poloidal coordinate of the simulated flux tube for CIEMAT-QI4 at $\beta = 0\%$ (red areas), 2% (blue areas), and 4% (green areas).

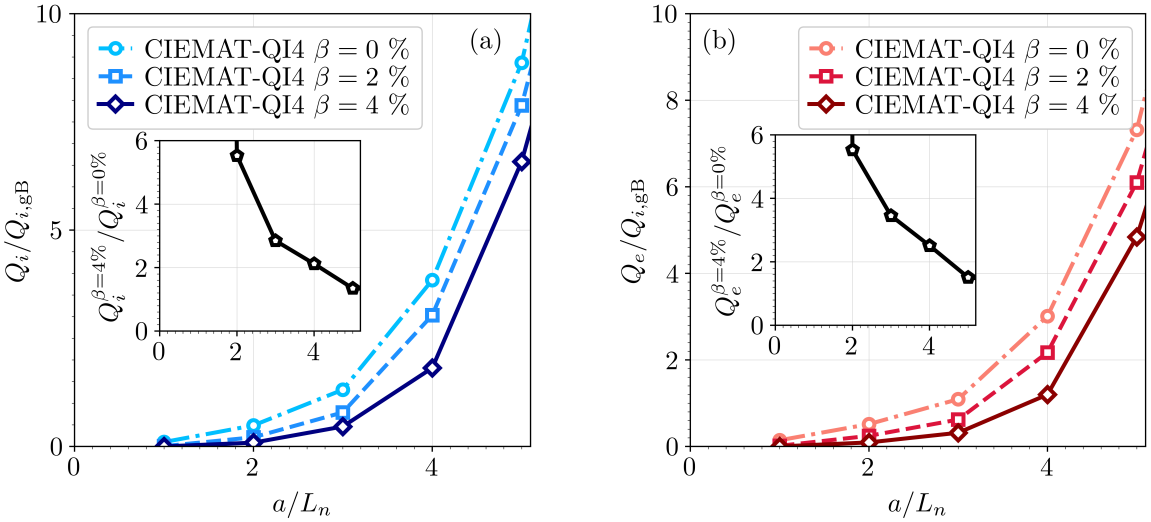

Figure 7. Main ion (a) and electron (b) heat flux as a function of the normalised density gradient for vanishing temperature gradient for both species, considering the CIEMAT-QI4 configuration at $\beta = 0\%$ (circles), 2% (squares), and 4% (diamonds). The inset in each figure depicts the ratio of their values at $\beta = 4\%$ to those at $\beta = 0\%$ for the corresponding ion or electron heat flux.

4(b), the electron heat (Q_e) and particle (Γ) fluxes, respectively, are presented. Both figures show a difference at low density gradient values not as significant as for the ion heat flux (figure 3(a)) but, still visible for $a/L_n \leq 1$ and Q_e. Again, as the density increases above $a/L_n = 3$ the curves of both devices separate from each other, with CIEMAT-QI4 maintaining lower levels of Q_e and Γ. As for Γ both configurations find a comparable level of inward turbulent flux at zero density gradient (turbulent pinch), that has been proven to counteract effectively the neoclassical thermo-diffusion responsible for the tendency to density core depletion in stellarators [27]. As the density gradient increases, the particle flux increases at comparable rate up to $a/L_n = 3$, value from which CIEMAT-QI4 maintains a substantially lower particle flux than W7-X. The latter is important in view of the capacity of a configuration to support the formation of a density pedestal, an ingredient with a recognised role in the generation of transport barriers and access to high confinement mode.

Delving into the correlation between the proximity to maximum-J and turbulent transport, a scan has been performed on the density gradient, considering CIEMAT-QI4 at three different values of the normalised plasma pressure, β. Prior to the presentation of the results, it is important to recall that the configuration gets closer to exactly satisfying the maximum-J property as β increases This can be observed in figure 5. We will focus on turbulent transport driven exclusively by the density gradient because theory predicts that density-gradient-driven TEM are stable in exactly maximum-J configurations [16, 17]. Thus, vanishing values of the ion and electron temperature gradients have been taken. Looking at the coefficient $\mathcal{K}_\alpha$ along the parallel coordinate of the simulated flux tubes, rep-

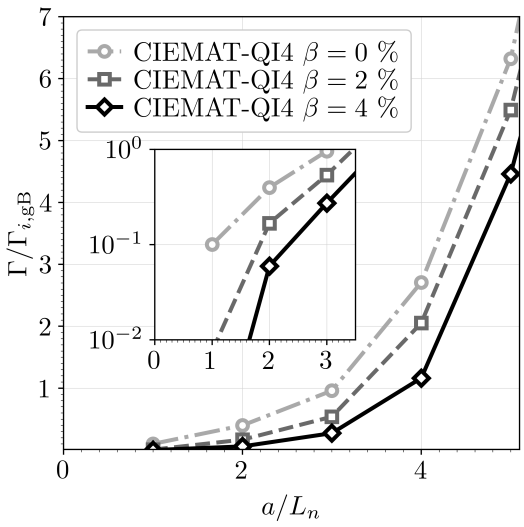

Figure 8. Turbulent particle flux as a function of the normalised density gradient for vanishing ion and electron temperature gradients, considering CIEMAT-QI4 at $\beta = 0\%$ (circles), 2% (squares), and 4% (diamonds). The inset displays a logarithmic scale zoom focusing on the lowest values of the density gradient within the scanned range.

resented in the the figure 6, one can also observe that the differences between CIEMAT-QI4 at different values of β are very pronounced for this parameter in particular. Not only for the transition from $\beta = 0\%$ to 2% the areas of bad curvature shrink, but also for the transition from $\beta = 2\%$ to 4%. The results of this scan are shown in figures 7(a) for the ion heat flux, figure 7(b) for the electron heat flux and figure 8 for the particle flux.

The three fluxes follow apparently an exponential increase with the density gradient. It is also observed that, indeed, the increase in β produces significantly lower fluxes. Looking at the insets of figures 7(a) and 7(b), which represent the ratio between the corresponding heat flux at $\beta = 0\%$ and $\beta = 4\%$, it is observed that the difference factor between the two becomes increasingly larger with decreasing a/L_n. For $a/L_n = 5$, the heat fluxes at $\beta = 4\%$ are 1.5 lower than for $\beta = 0\%$, while that factor increases up to nearly 6 for $a/L_n = 2.0$. Because the case $\beta = 4\%$ is marginally unstable at $a/L_n = 1$ the ratio $Q_s^{\beta=0\%}/Q_s^{\beta=4\%}$ approaches off-scale values near to one hundred. Finally, looking at the particle flux, Γ, the exponential trend with a/L_n, common to those just discussed for Q_i and Q_e, points out the stiff character of particle transport. Analogously to the scaling derived for the heat flux versus the temperature gradient from critical balance arguments [37], the trend of the particle flux versus the density gradient can be quantified. Fitting the particle flux to the functional form $\Gamma = K_1(a/L_n)^{K_2}$ results in exponents of around $K_2 \sim 4$, see table 1 for the specific values of the coefficients K_1 and K_2 for each case of β. For this fitting, only the cases with $a/L_n \geq 2$ of well developed turbulence have been considered. The particle flux at lower gradients, isolated in figure 8 (inset) using logarithmic scale, shows how $\Gamma(a/L_n)$ tends to critical gradients significantly larger as β increases. In summary, the simulations for CIEMAT-QI4 at different values of β show that the greater the value of β and, consequently, the closer to maximum-J, the lower the transport driven by electrostic turbulence and the larger its critical density gradient.

β [%]	K_1	K_2
0.0	$(1.3 \pm 0.2) \times 10^{-2}$	3.85 ± 0.09
2.0	$(0.7 \pm 0.1) \times 10^{-2}$	4.12 ± 0.09
4.0	$(0.2 \pm 0.1) \times 10^{-2}$	4.7 ± 0.3

Table 1. Results from fitting the particle fluxes with $a/L_n \leq 3$ represented in figure 8 to a function with the form $\Gamma = K_1(a/L_n)^{K_2}$.

4. Conclusions

CIEMAT-QI4 is a quasi-isodynamic configuration that approximately satisfies the maximum-J condition even at small plasma β. CIEMAT-QI4 was introduced in [10], where it was shown that it exhibits very good fast-ion confinement for a broad range of β values, gives reduced neoclassical transport and small bootstrap current, and is ideal MHD stable up to $\beta = 5\%$. In the present paper we have reported a first numerical analysis of turbulent transport for the CIEMAT-QI4 configuration by means of nonlinear electrostatic gyrokinetic simulations performed with the code `stella` [24].

A scan of the turbulent heat fluxes in the density gradient, keeping finite values of the ion and electron temperature gradients, shows that CIEMAT-QI4 features: 1) low turbulent heat fluxes at flat or weakly peaked density profiles. In particular, it has been shown that the configuration is resilient to the strong increase in the heat flux typically produced by introducing kinetic electrons [30, 18]; 2) the turbulent heat fluxes remain low and weakly dependent on the density gradient at moderate values thereof; 3) the fluxes increase very mildly when going to strongly peaked density profiles, as expected from analytical arguments relating resistance to density-gradient-driven trapped-electron-mode instabilities and proximity to the maximum-J property [16, 17]. In summary, CIEMAT-QI4 exhibits reduced turbulent transport in wide experimentally relevant regions of parameter space.

In addition, turbulent transport driven solely by density-gradient-driven trapped-electron-modes has been investigated in CIEMAT-QI4 for different values of β, (motivated, on the one hand, by the fact that in quasi-isodynamic configurations, and therefore in CIEMAT-QI4, the larger β the closer the configuration is to satisfying the maximum-J property. And, on the other hand, by the analytical results [16, 17] that predict stability of density-gradient-driven trapped-electron-modes for exactly maximum-J configurations). Although with comparable stiffness, turbulent fluxes are significantly lower at higher β and tend to larger critical gradients.

In the future, it will be necessary to study how the reduction in the turbulent fluxes reported in this paper translates into the equilibrium profiles determined by transport calculations [38] and how electromagnetic effects modify the results at high β [39, 40].

Acknowledgements

J.M.G.R. is grateful to A. Bañón Navarro for fruitful discussions and Michael Barnes for his support with the code `stella`. This work has been carried out within the framework of the EUROfusion Consortium, funded by the European Union via the Euratom Research and Training Programme (Grant Agreement No 101052200 – EUROfusion). Views and opinions expressed are however those of the author(s) only and do not necessarily reflect those of the European Union or the European Commission. Neither the European Union nor the European Commission can be held responsible for them. This research was supported in part by grant PID2021-123175NB-I00, Ministerio de Ciencia e Innovación, Spain. Simulations were performed in the supercomputers Marconi (CINECA, Italy) under the `FUA_STELTURB` project of the *TSVV#13 Task Stellarator Turbulence Simulation.*

Bibliography

[1] P Helander. Theory of plasma confinement in non-axisymmetric magnetic fields. *Rep. Prog. Phys.*, 77:087001, 2014.

[2] F. Simon B. Anderson, Abdulgader F. Almagri, David T. Anderson, Peter G. Matthews, Joseph N. Talmadge, and J. Leon Shohet. The helically symmetric experiment, (hsx) goals, design and status. *Fusion Technology*, 27(3T):273–277, April 1995.

[3] M C Zarnstorff, L A Berry, A Brooks, E Fredrickson, G-Y Fu, S Hirshman, S Hudson, L-P Ku, E Lazarus, D Mikkelsen, D Monticello, G H Neilson, N Pomphrey, A Reiman, D Spong, D Strickler, A Boozer, W A Cooper, R Goldston, R Hatcher, M Isaev, C Kessel, J Lewandowski, J F Lyon, P Merkel, H Mynick, B E Nelson, C Nuehrenberg, M Redi, W Reiersen, P Rutherford, R Sanchez, J Schmidt, and R B White. Physics of the compact advanced stellarator NCSX. *Plasma Physics and Controlled Fusion*, 43(12A):A237–A249, November 2001.

[4] Matt Landreman and Elizabeth Paul. Magnetic fields with precise quasisymmetry for plasma confinement. *Physical Review Letters*, 128(3), January 2022.

[5] Matt Landreman and Peter J. Catto. Omnigenity as generalized quasisymmetry. *Physics of Plasmas*, 19(5), March 2012.

[6] C. D. Beidler, H. M. Smith, A. Alonso, T. Andreeva, J. Baldzuhn, M. N. A. Beurskens, M. Borchardt, S. A. Bozhenkov, K. J. Brunner, H. Damm, M. Drevlak, O. P. Ford, G. Fuchert, J. Geiger, P. Helander, U. Hergenhahn, M. Hirsch, U. Höfel, Ye. O. Kazakov, R. Kleiber, M. Krychowiak, S. Kwak, A. Langenberg, H. P. Laqua, U. Neuner, N. A. Pablant, E. Pasch, A. Pavone, T. S. Pedersen, K. Rahbarnia, J. Schilling, E. R. Scott, T. Stange, J. Svensson, H. Thomsen, Y. Turkin, F. Warmer, R. C. Wolf, D. Zhang, I. Abramovic, S. Äkäslompolo, J. Alcusón, P. Aleynikov, K. Aleynikova, A. Ali, A. Alonso, G. Anda, E. Ascasibar, J. P. Bähner, S. G. Baek, M. Balden, M. Banduch, T. Barbui, W. Behr, A. Benndorf, C. Biedermann, W. Biel, B. Blackwell, E. Blanco, M. Blatzheim, S. Ballinger, T. Bluhm, D. Böckenhoff, B. Böswirth, L.-G. Böttger, V. Borsuk, J. Boscary, H.-S. Bosch, R. Brakel, H. Brand, C. Brandt, T. Bräuer, H. Braune, S. Brezinsek, K.-J. Brunner, R. Burhenn, R. Bussiahn, B. Buttenschön, V. Bykov, J. Cai, I. Calvo, B. Cannas, A. Cappa, A. Carls, L. Carraro, B. Carvalho, F. Castejon, A. Charl, N. Chaudhary, D. Chauvin, F. Chernyshev, M. Cianciosa, R. Citarella, G. Claps, J. Coenen, M. Cole, M. J. Cole, F. Cordella, G. Cseh, A. Czarnecka, K. Czerski, M. Czerwinski, G. Czymek, A. da Molin, A. da Silva, A. de la Pena, S. Degenkolbe, C. P. Dhard, M. Dibon, A. Dinklage, T. Dittmar, P. Drewelow, P. Drews, F. Durodie, E. Edlund, F. Effenberg, G. Ehrke, S. Elgeti, M. Endler, D. Ennis, H. Esteban, T. Estrada, J. Fellinger, Y. Feng, E. Flom, H. Fernandes, W. H. Fietz, W. Figacz, J. Fontdecaba, T. Fornal, H. Frerichs, A. Freund, T. Funaba, A. Galkowski, G. Gantenbein, Y. Gao, J. García Regaña, D. Gates, B. Geiger, V. Giannella, A. Gogoleva, B. Goncalves, A. Goriaev, D. Gradic, M. Grahl, J. Green, H. Greuner, A. Grosman, H. Grote, M. Gruca, O. Grulke, C. Guerard, P. Hacker, X. Han, J. H. Harris, D. Hartmann, D. Hathiramani, B. Hein, B. Heinemann, P. Helander, S. Henneberg, M. Henkel, U. Hergenhahn, J. Hernandez Sanchez, C. Hidalgo, K. P. Hollfeld, A. Hölting, D. Höschen, M. Houry, J. Howard, X. Huang, Z. Huang, M. Hubeny, M. Huber, H. Hunger, K. Ida, T. Ilkei, S. Illy, B. Israeli, S. Jablonski, M. Jakubowski, J. Jelonnek, H. Jenzsch, T. Jesche, M. Jia, P. Junghanns, J. Kacmarczyk, J.-P. Kallmeyer, U. Kamionka, H. Kasahara, W. Kasparek, N. Kenmochi, C. Killer, A. Kirschner, T. Klinger, J. Knauer, M. Knaup, A. Knieps, T. Kobarg, G. Kocsis, F. Köchl, Y. Kolesnichenko, A. Könies, R. König, P. Kornejew, J.-P. Koschinsky, F. Köster, M. Krämer, R. Krampitz, A. Krämer-Flecken, N. Krawczyk, T. Kremeyer, J. Krom, I. Ksiazek, M. Kubkowska, G. Kühner, T. Kurki-Suonio, P. A. Kurz, M. Landreman, P. Lang, R. Lang, S. Langish, H. Laqua, R. Laube, S. Lazerson, C. Lechte, M. Lennartz, W. Leonhardt, C. Li, C. Li, Y. Li, Y. Liang, C. Linsmeier, S. Liu, J.-F. Lobsien, D. Loesser, J. Loizu Cisquella, J. Lore, A. Lorenz, M. Losert, A. Lücke, A. Lumsdaine, V. Lutsenko, H. Maaßberg, O. Marchuk, J. H. Matthew, S. Marsen, M. Marushchenko, S. Masuzaki, D. Maurer, M. Mayer, K. McCarthy, P. McNeely, A. Meier, D. Mellein, B. Mendelevitch, P. Mertens, D. Mikkelsen, A. Mishchenko, B. Missal, J. Mittelstaedt, T. Mizu-

uchi, A. Mollen, V. Moncada, T. Mönnich, T. Morisaki, D. Moseev, S. Murakami, G. Náfrádi, M. Nagel, D. Naujoks, H. Neilson, R. Neu, O. Neubauer, T. Ngo, D. Nicolai, S. K. Nielsen, H. Niemann, T. Nishizawa, R. Nocentini, C. Nührenberg, J. Nührenberg, S. Obermayer, G. Offermanns, K. Ogawa, J. Ölmanns, J. Ongena, J. W. Oosterbeek, G. Orozco, M. Otte, L. Pacios Rodriguez, N. Panadero, N. Panadero Alvarez, D. Papenfuß, S. Paqay, E. Pawelec, T. S. Pedersen, G. Pelka, V. Perseo, B. Peterson, D. Pilopp, S. Pingel, F. Pisano, B. Plaum, G. Plunk, P. Pölöskei, M. Porkolab, J. Proll, M.-E. Puiatti, A. Puig Sitjes, F. Purps, M. Rack, S. Récsei, A. Reiman, F. Reimold, D. Reiter, F. Remppel, S. Renard, R. Riedl, J. Riemann, K. Risse, V. Rohde, H. Röhlinger, M. Romé, D. Rondeshagen, P. Rong, B. Roth, L. Rudischhauser, K. Rummel, T. Rummel, A. Runov, N. Rust, L. Ryc, S. Ryosuke, R. Sakamoto, M. Salewski, A. Samartsev, E. Sánchez, F. Sano, S. Satake, J. Schacht, G. Satheeswaran, F. Schauer, T. Scherer, A. Schlaich, G. Schlisio, F. Schluck, K.-H. Schlüter, J. Schmitt, H. Schmitz, O. Schmitz, S. Schmuck, M. Schneider, W. Schneider, P. Scholz, R. Schrittwieser, M. Schröder, T. Schröder, R. Schroeder, H. Schumacher, B. Schweer, S. Sereda, B. Shanahan, M. Sibilia, P. Sinha, S. Sipliä, C. Slaby, M. Sleczka, W. Spiess, D. A. Spong, A. Spring, R. Stadler, M. Stejner, L. Stephey, U. Stridde, C. Suzuki, V. Szabó, T. Szabolics, T. Szepesi, Z. Szökefalvi-Nagy, N. Tamura, A. Tancetti, J. Terry, J. Thomas, M. Thumm, J. M. Travere, P. Traverso, J. Tretter, H. Trimino Mora, H. Tsuchiya, T. Tsujimura, S. Tulipán, B. Unterberg, I. Vakulchyk, S. Valet, L. Vanó, P. van Eeten, B. van Milligen, A. J. van Vuuren, L. Vela, J.-L. Velasco, M. Vergote, M. Vervier, N. Vianello, H. Viebke, R. Vilbrandt, A. von Stechow, A. Vorköper, S. Wadle, F. Wagner, E. Wang, N. Wang, Z. Wang, T. Wauters, L. Wegener, J. Weggen, T. Wegner, Y. Wei, G. Weir, J. Wendorf, U. Wenzel, A. Werner, A. White, B. Wiegel, F. Wilde, T. Windisch, M. Winkler, A. Winter, V. Winters, S. Wolf, R. C. Wolf, A. Wright, G. Wurden, P. Xanthopoulos, H. Yamada, I. Yamada, R. Yasuhara, M. Yokoyama, M. Zanini, M. Zarnstorff, A. Zeitler, H. Zhang, J. Zhu, M. Zilker, A. Zocco, S. Zoletnik, and M. Zuin. Publisher correction: Demonstration of reduced neoclassical energy transport in Wendelstein 7-X. *Nature*, 598(7882):E5–E5, October 2021.

[7] A. Dinklage, C. D. Beidler, P. Helander, G. Fuchert, H. Maaßberg, K. Rahbarnia, T. Sunn Pedersen, Y. Turkin, R. C. Wolf, A. Alonso, T. Andreeva, B. Blackwell, S. Bozhenkov, B. Buttenschön, A. Czarnecka, F. Effenberg, Y. Feng, J. Geiger, M. Hirsch, U. Höfel, M. Jakubowski, T. Klinger, J. Knauer, G. Kocsis, A. Krämer-Flecken, M. Kubkowska, A. Langenberg, H. P. Laqua, N. Marushchenko, A. Mollén, U. Neuner, H. Niemann, E. Pasch, N. Pablant, L. Rudischhauser, H. M. Smith, O. Schmitz, T. Stange, T. Szepesi, G. Weir, T. Windisch, G. A. Wurden, and D. Zhang. Magnetic configuration effects on the Wendelstein 7-X stellarator. *Nature Physics*, 14(8):855–860, May 2018.

[8] J.L. Velasco, I. Calvo, S. Mulas, E. Sánchez, F.I. Parra, Á. Cappa, and the W7-X Team. A model for the fast evaluation of prompt losses of energetic ions in stellarators. *Nuclear Fusion*, 61(11):116059, October 2021.

[9] M.N.A. Beurskens, S.A. Bozhenkov, O. Ford, P. Xanthopoulos, A. Zocco, Y. Turkin, A. Alonso, C. Beidler, I. Calvo, D. Carralero, T. Estrada, G. Fuchert, O. Grulke, M. Hirsch, K. Ida, M. Jakubowski, C. Killer, M. Krychowiak, S. Kwak, S. Lazerson, A. Langenberg, R. Lunsford, N. Pablant, E. Pasch, A. Pavone, F. Reimold, Th. Romba, A. von Stechow, H.M. Smith, T. Windisch, M. Yoshinuma, D. Zhang, R.C. Wolf, and the W7-X Team. Ion temperature clamping in Wendelstein 7-X electron cyclotron heated plasmas. *Nuclear Fusion*, 61(11):116072, October 2021.

[10] E. Sánchez, J.L. Velasco, I. Calvo, and S. Mulas. A quasi-isodynamic configuration with good confinement of fast ions at low plasma β. *Nuclear Fusion*, 63(6):066037, May 2023.

[11] Gabriel G. Plunk, Matt Landreman, and Per Helander. Direct construction of optimized stellarator shapes. Part 3. Omnigenity near the magnetic axis. *Journal of Plasma Physics*, 85(6), November 2019.

[12] R. Jorge, G.G. Plunk, M. Drevlak, M. Landreman, J.-F. Lobsien, K. Camacho Mata, and P. Helander. A single-field-period quasi-isodynamic stellarator. *Journal of Plasma Physics*, 88(5), September 2022.

[13] Katia Camacho Mata, Gabriel G. Plunk, and R. Jorge. Direct construction of stellarator-symmetric quasi-isodynamic magnetic configurations. *Journal of Plasma Physics*, 88(5), October 2022.

[14] A.G. Goodman, K. Camacho Mata, S.A. Henneberg, R. Jorge, M. Landreman, G.G. Plunk, H.M. Smith, R.J.J. Mackenbach, C.D. Beidler, and P. Helander. Constructing precisely quasi-isodynamic magnetic fields. *Journal of Plasma Physics*, 89(5), September 2023.

[15] J.L. Velasco, I. Calvo, E. Sánchez, and F.I. Parra. Robust stellarator optimization via flat mirror magnetic fields. *Nuclear Fusion*, 63(12):126038, October 2023.

[16] Marshall N. Rosenbluth. Low-frequency limit of interchange instability. *The Physics of Fluids*, 11(4):869–872, April 1968.

[17] P. Helander, J. H. E. Proll, and G. G. Plunk. Collisionless microinstabilities in stellarators. i. analytical theory of trapped-particle modes. *Physics of Plasmas*, 20(12):122505, December 2013.

[18] J.H.E. Proll, G.G. Plunk, B.J. Faber, T. Görler, P. Helander, I.J. McKinney, M.J. Pueschel, H.M. Smith, and P. Xanthopoulos. Turbulence mitigation in maximum-J stellarators with electron-density gradient. *Journal of Plasma Physics*, 88(1), February 2022.

[19] G. G. Plunk, J. W. Connor, and P. Helander. Collisionless microinstabilities in stellarators. part 4. the ion-driven trapped-electron mode. *Journal of Plasma Physics*, 83(4), August 2017.

[20] Samuel Lazerson, John Schmitt, Caoxiang Zhu, Joshua Breslau, and All STELLOPT Developers. Stellopt, 2020.

[21] J.L. Velasco, I. Calvo, F.I. Parra, and J.M. García-Regaña. KNOSOS: A fast orbit-averaging neoclassical code for stellarator geometry. *Journal of Computational Physics*, 418:109512, October 2020.

[22] R C Grimm, R L Dewar, and J Manickam. Ideal MHD stability calculations in axisymmetric toroidal coordinate systems. *Journal of Computational Physics*, 49:94, 1983.

[23] S. P. Hirshman and H. K. Meier. Optimized fourier representations for three-dimensional magnetic surfaces. *Physics of Fluids*, 28(5):1387, 1985.

[24] M. Barnes, F.I. Parra, and M. Landreman. stella: An operator-split, implicit–explicit δf-gyrokinetic code for general magnetic field configurations. *Journal of Computational Physics*, 391:365–380, 02 2019.

[25] M. Maurer, A. Bañón Navarro, T. Dannert, M. Restelli, F. Hindenlang, T. Görler, D. Told, D. Jarema, G. Merlo, and F. Jenko. GENE-3D: A global gyrokinetic turbulence code for stellarators. *Journal of Computational Physics*, 420:109694, November 2020.

[26] N. R. Mandell, W. Dorland, I. Abel, R. Gaur, P. Kim, M. Martin, and T. Qian. Gx: a gpu-native gyrokinetic turbulence code for tokamak and stellarator design, 2022.

[27] H. Thienpondt, J. M. García-Regaña, I. Calvo, J. A.

Alonso, J. L. Velasco, A. González-Jerez, M. Barnes, K. Brunner, O. Ford, G. Fuchert, J. Knauer, E. Pasch, and L. Vanó. Prevention of core particle depletion in stellarators by turbulence. *Physical Review Research*, 5(2), June 2023.

[28] J. M. García-Regaña, M. Barnes, I. Calvo, F. I. Parra, J. A. Alcusón, R. Davies, A. González-Jerez, A. Mollén, E. Sánchez, J. L. Velasco, and A. Zocco. Turbulent impurity transport simulations in Wendelstein 7-X plasmas. *Journal of Plasma Physics*, 87(1), February 2021.

[29] J.M. García-Regaña, M. Barnes, I. Calvo, A. González-Jerez, H. Thienpondt, E. Sánchez, F. I. Parra, and D. A. St.-Onge. Turbulent transport of impurities in 3d devices. *Nuclear Fusion*, 61(11):116019, September 2021.

[30] H. Thienpondt, J. M. García-Regaña, I. Calvo, G. Acton, and M. Barnes. Influence of the density gradient at ion-scales: an intermachine study with the gyrokinetic code stella, 2024.

[31] S.A. Bozhenkov, Y. Kazakov, O.P. Ford, M.N.A. Beurskens, J. Alcusón, J.A. Alonso, J. Baldzuhn, C. Brandt, K.J. Brunner, H. Damm, G. Fuchert, J. Geiger, O. Grulke, M. Hirsch, U. Höfel, Z. Huang, J. Knauer, M. Krychowiak, A. Langenberg, H.P. Laqua, S. Lazerson, N. B. Marushchenko, D. Moseev, M. Otte, N. Pablant, E. Pasch, A. Pavone, J.H.E. Proll, K. Rahbarnia, E.R. Scott, H.M. Smith, T. Stange, A. von Stechow, H. Thomsen, Yu. Turkin, G. Wurden, P. Xanthopoulos, D. Zhang, and R.C. Wolf and. High-performance plasmas after pellet injections in Wendelstein 7-X. *Nuclear Fusion*, 60(6):066011, May 2020.

[32] M F Martin, M Landreman, P Xanthopoulos, N R Mandell, and W Dorland. The parallel boundary condition for turbulence simulations in low magnetic shear devices. *Plasma Physics and Controlled Fusion*, 60(9):095008, July 2018.

[33] A. González-Jerez, P. Xanthopoulos, J.M. García-Regaña, I. Calvo, J. Alcusón, A. Bañón Navarro, M. Barnes, F.I. Parra, and J. Geiger. Electrostatic gyrokinetic simulations in Wendelstein 7-X geometry: benchmark between the codes stella and GENE. *Journal of Plasma Physics*, 88(3), June 2022.

[34] D. Carralero, T. Estrada, E. Maragkoudakis, T. Windisch, J.A. Alonso, M. Beurskens, S. Bozhenkov, I. Calvo, H. Damm, O. Ford, G. Fuchert, J.M. García-Regaña, N. Pablant, E. Sánchez, E. Pasch, J.L. Velasco, and the Wendelstein 7-X team. An experimental characterization of core turbulence regimes in Wendelstein 7-X. *Nuclear Fusion*, 61(9):096015, August 2021.

[35] T. Romba, F. Reimold, R.J.E. Jaspers, O.P. Ford, L. Vanó, and T. Klinger. Suppression of anomalous impurity transport in NBI-heated w7-x plasmas. *Nuclear Fusion*, 63(7):076023, June 2023.

[36] H. Thienpondt, J. M. García-Regaña, I. Calvo, A. González-Jerez, M. Barnes, F. I. Parra, and R. Davies. Turbulent transport versus density gradient: an inter-machine study with the gyrokinetic code stella. In *International Stellarator and Heliotron Workshop, Warsaw*, 2022.

[37] M. Barnes, F. I. Parra, and A. A. Schekochihin. Critically balanced ion temperature gradient turbulence in fusion plasmas. *Physical Review Letters*, 107(11), September 2011.

[38] A. Bañón Navarro, A. Di Siena, J.L. Velasco, F. Wilms, G. Merlo, T. Windisch, L.L. LoDestro, J.B. Parker, and F. Jenko. First-principles based plasma profile predictions for optimized stellarators. *Nuclear Fusion*, 63(5):054003, March 2023.

[39] K. Aleynikova, A. Zocco, P. Xanthopoulos, P. Helander, and C. Nührenberg. Kinetic ballooning modes in tokamaks and stellarators. *Journal of Plasma Physics*, 84(6), December 2018.

[40] Felix Wilms, Alejandro Bañón Navarro, Gabriele Merlo, Leonhard Leppin, Tobias Görler, Tilman Dannert, Florian Hindenlang, and Frank Jenko. Global electromagnetic turbulence simulations of w7-x-like plasmas with GENE-3D. *Journal of Plasma Physics*, 87(6), November 2021.